

PHYSICAL PROPERTIES AND KINETIC STRUCTURE OF A STARLESS CORE IN THE TAURUS MOLECULAR CLOUD

HIROKO SHINNAGA

Harvard-Smithsonian Center for Astrophysics, Submillimeter Array, P.O. Box 824,
Hilo, HI 96721; hshinnaga@cfa.harvard.edu

NAGAYOSHI OHASHI

Institute of Astronomy and Astrophysics, Academia Sinica, P.O. Box 23-141, Taipei 106, Taiwan

SIOW-WANG LEE

Department of Astronomy and Astrophysics, University of Toronto, 60 St. George
Street, Toronto, ON M5S 3H8, Canada

AND

GERALD H. MORIARTY-SCHIEVEN

National Research Council of Canada, Joint Astronomy Centre, 660 North A'ohoku
Place, University Park, Hilo HI 96720

Received 2002 November 11; accepted 2003 September 10

ABSTRACT

We have made synthesis imaging of a starless core in the Taurus molecular cloud L1521F, with two key chemical evolutionary tracers, CCS ($J_N = 3_2 - 2_1$), which traces young evolutionary phase of cores, and N_2H^+ ($J = 1 - 0$), which traces until the late evolutionary phase, as well as mapping observations of submillimeter dust continuum. The peak positions, as well as the radial distributions, of N_2H^+ and dust continuum coincide with each other. Unlike the other tracers, CCS shows a dip at the dust continuum center, suggesting that the abundance of the molecule decreases at the core center because of depletion and chemical reactions. The channel maps of both molecular lines clearly revealed clumpy substructures inside the core. Using an automatic and objective routine, eight and four clumps have been identified in the CCS and N_2H^+ channel maps, respectively. The abundances of the molecules are estimated toward the dust continuum center. Using our derived abundances, the LTE masses for each clump are estimated. The CCS components, which appear to trace the envelope, show an overall velocity gradient from east to west, whereas a N_2H^+ clump located at the core center shows a gradient from west to east. Assuming that the velocity gradients are due to rotation, the observational results indicate that the rotation of the outer envelope (size $\lesssim 0.08$ pc $\sim 16,000$ AU) and that of the central compact region (size $\lesssim 0.03$ pc ~ 6000 AU) have different axes with almost opposite senses of rotation. The velocity gradients of the southern and northern CCS components are estimated to be 7.2 and 9.2 km s $^{-1}$ pc $^{-1}$ at size scales of 0.05 and 0.04 pc, respectively. The velocity gradient of the N_2H^+ components at the core center is estimated to be 15 km s $^{-1}$ pc $^{-1}$ at a size scale of 0.01 pc (~ 2000 AU). Examining the line width–size correlation of these clumps and of other cold (kinetic temperature $T_K \lesssim 10$ K) starless cores, the slope index is found to be slightly shallower than those values for cores containing stars. Assuming a spherical, homogeneous sphere, the ratios of rotational to gravitational energy, β , of these cores are calculated to be ~ 0.3 for the CCS and ~ 1.0 for the N_2H^+ components, respectively. The relation of the specific angular momentum (J/M) to size seen at scales larger than ~ 0.03 pc (~ 6000 AU) appears to flatten out at sizes smaller than ~ 6000 AU, for which the specific angular momentum is relatively constant at ~ 0.002 . This is consistent with results reported by Ohashi et al. Based on a chemical evolutionary model, the core may be in a young starless cores phase, assuming that the dip of CCS at the core center is caused by depletion and chemical reaction. L1521F may be in a younger starless-core phase than L1544.

Subject headings: ISM: clouds — ISM: individual (L1521F) — ISM: molecules — radio lines: ISM — stars: formation

1. INTRODUCTION

The first stage of star formation starts from a process of contraction of starless cores, which are compact (size ~ 0.1 pc, i.e., $\sim 2 \times 10^4$ AU), cold (kinetic temperature $T_K \lesssim 10$ K), and dense (gas number density $n \sim 10^4$) condensations (Ho, Barrett, & Martin 1978; Churchwell, Winnewisser, & Walmsley 1978; Myers, Ho, & Benson 1979; Ungerechts, Walmsley, & Winnewisser 1980; Snell 1981). Starless cores thus are targets for studying the initial conditions of star formation before stars form inside them.

The evolutionary sequence of cores with stars is well described empirically by their spectral energy distribution (SED) (Lada 1987). This is supported by theoretical models (Adams, Lada, & Shu 1987). André, Ward-Thompson, & Barsony (1993) extended it to a younger phase, naming it the Class 0 phase. The phase is characterized by the existence of a deeply embedded infrared source with its SED corresponding to a bolometric temperature of $\lesssim 70$ K.

On the other hand, the earliest evolutionary stage of star formation, i.e., the phase of starless dense cores, is still not well understood. In particular, the initial conditions of star

formation are critical in determining fragmentation, contraction, stellar mass, and the timescales and structures for each evolutionary phase. In order to understand how stars form in dense cores, it is crucial to investigate their physical properties and kinetic structures at different evolutionary stages. Detailed imaging observations to investigate such structures can test the validity of theoretical models (e.g., Larson 1969 and Penston 1969 [purely dynamical isothermal collapse with spherical symmetry]; Shu 1977 [inside-out collapse model for a singular isothermal sphere]; McLaughlin & Pudritz 1997 [a logotropic sphere model]).

So far, a few starless cores have been studied extensively by observing several molecular lines and dust continuum. Dense cores in the Taurus molecular cloud (TMC) are good targets for studying low-mass star formation because the TMC is relatively nearby, at a distance of 140 pc (Elias 1978). L1544 in the TMC is one of the starless cores that has been investigated in great detail. The strong self-absorption feature of the CS $J = 2 - 1$ transition shows a global pattern of infall motion (Tafalla et al. 1998). N_2H^+ interferometric observations show a slowly contracting feature (Williams et al. 1999). CCS interferometric observation reveal infall and rotation in the envelope (Ohashi et al. 1999). OH Zeeman observations toward the source have found a magnetic field strength of $B_{LOS} = +11 \pm 2 \mu\text{G}$ (Crutcher & Troland 2000). The degree of linear polarization in the submillimeter continuum is measured to be $0.93\% \pm 0.27\%$ (Ward-Thompson et al. 2000). Depletion of CS, CCS, and CO at densities above $\sim 10^5 \text{ cm}^{-3}$ (Caselli et al. 1999; Ohashi et al. 1999; Tafalla et al. 2002; Lee et al. 2003) and deuterium fractionation of a couple of molecules (e.g., N_2D^+ [Caselli et al. 2002] and H_2D^+ [Caselli et al. 2003]) have been observed in the core. Chemical evolutionary models of the core are discussed (Aikawa et al. 2001; Li et al. 2002). While many detailed studies of L1544 core have been reported, other detailed examples of starless cores are also greatly needed in order to interpret them with stronger statistical confidence and in order to extend them toward investigating the evolution of starless cores, as well as understanding the whole picture of the star formation process.

We report here a detailed study of L1521F, another dense starless core in the TMC (Codella et al. 1997). This source has already been mapped with the (J, K) = (1, 1) lines of NH_3 and $HC_3N J = 5 - 4$ line using the MPIFR 100 m antenna (Codella et al. 1997), $H^{13}CO^+ J = 1 - 2$ (Mizuno et al. 1994) with the Nobeyama 45 m telescope, and $C^{18}O J = 1 - 0$ taken with the Nagoya 4 m telescope (Onishi et al. 1996). Onishi, Mizuno, & Fukui (1999) reported observations of higher rotational transitions of HCO^+ and the isotope $H^{13}CO^+$ with the CSO (Caltech Submillimeter Telescope) toward the core center and revealed the high density of 10^6 cm^{-3} within $\sim 1000 \text{ AU}$ at the center and estimated a very short dynamical timescale of $\sim 10^4 \text{ yr}$. Lee, Myers, & Tafalla (1999) reported the CS $J = 2 - 1$ and $N_2H^+ J = 1 - 0$ spectra toward the core center using the NEROC Haystack 37 m telescope. The $C^{18}O$ observation (Onishi et al. 1996) traces a large size core (the radius of which is 0.16 pc) with a mass of $9.4 M_\odot$. The $H^{13}CO^+$ observation with $20''$ spatial resolution revealed a $3 M_\odot$ core with a radius of 0.1 pc (Mizuno et al. 1994). From the ammonia (1, 1) observations (Codella et al. 1997), the mass of the core had been estimated to be $0.7 M_\odot$ with the radius of $\sim 0.08 \text{ pc}$ and $n(H_2)$ of $\sim 2 \times 10^5 \text{ cm}^{-3}$. Here we report the results of imaging observations of CCS $J_N = 3_2 - 2_1$ and $N_2H^+ J = 1 - 0$ transitions with higher angular and frequency resolutions, together with an image of the dust continuum emission at a submillimeter wavelength.

2. OBSERVATION

2.1. Millimeter-Wave Observations

We made imaging observations with the CCS $J_N = 3_2 - 2_1$ (33.751374 GHz; Yamamoto et al. 1990) and $N_2H^+ J = 1 - 0$ transitions (93.17 GHz; Cazoli et al. 1985) toward L1521F using the Berkeley-Illinois-Maryland Association (BIMA) array¹ in 1998. The parameters of the observations are summarized in Table 1. The observations were conducted in the B+D configurations for CCS and in the C configuration for the N_2H^+ observations. For the CCS imaging, we used low-noise receivers utilizing cooled HEMT amplifiers that were developed for observations of the Sunyaev-Zeldovich effect (Carlstrom, Marshall, & Grego 1996). Spectral information was obtained using a digital correlator with 1024 channels and a total bandwidth of 6.25 MHz, providing a velocity resolution of 0.054 km s^{-1} for the CCS and 0.039 km s^{-1} for the N_2H^+ observations. The fields of view are $5'$ and $1/8'$ for CCS and N_2H^+ , respectively. The projected baselines for CCS range from 0.8 to 26.8 k λ , so that the resultant CCS images are insensitive to structures extended more than $4/3$, corresponding to $\sim 28,000 \text{ AU}$ at a distance of 140 pc. For the N_2H^+ observations, the projected baselines range from 1.8 to 25.1 k λ , so that the N_2H^+ images reported here are insensitive to structures extended more than $1/9$, corresponding to $\sim 14,000 \text{ AU}$ at the distance, 140 pc. The imaging data were analyzed by the MIRIAD package. The phase was calibrated by observing 0530+135, and the complex passband of each baseline was determined from observations of 3C 84. When CCS and N_2H^+ maps were made and cleaned, a Gaussian taper was applied to the visibility data to improve sensitivity to the extended low brightness emission. The resultant beam sizes have similar size scales, i.e., $17''.9 \times 16''.8$ with a position angle of -34° for CCS and $19''.9 \times 16''.4$ with a position angle of -56° for N_2H^+ . Note that the beam size of N_2H^+ shown in this paper is made to be almost the same size as CCS to improve the signal-to-noise ratio of N_2H^+ maps and for comparison between two molecular components with the same size scale. The 1σ noise levels for the channel maps are typically $170 \text{ mJy beam}^{-1}$ for CCS and $720 \text{ mJy beam}^{-1}$ for N_2H^+ . The conversion factors from flux density to brightness temperature are 3.57 K Jy^{-1} for CCS and 0.432 K Jy^{-1} for N_2H^+ , respectively. For the total intensity maps, the noise levels at 1σ are 70 mJy beam^{-1} for CCS and $170 \text{ mJy beam}^{-1}$ for N_2H^+ . In order to assess the kinetic structure of the N_2H^+ component, the $JF_1F = 101 - 012$ component is used (among seven hyperfine components; see Table 1) because it is isolated from the other components in frequency, so that one can assess the velocity structure free from mixing multiple transitions. All maps and spectra of N_2H^+ shown in this paper are for the $JF_1F = 101 - 012$ component. In order to adjust the center velocity of the main component of the N_2H^+ line, $JF_1F = 123 - 012$ transition, 8.047 km s^{-1} is added to the actual velocity of the isolated component, $JF_1F = 101 - 012$ transition, based on the results of the laboratory microwave spectroscopy (Cazoli et al. 1985).

To derive the optical depth of CCS and assess the missing flux, we observed the $J_N = 3_2 - 2_1$ lines of CCS and the isotope $CC^{34}S$ (33.111839 GHz; Yamamoto et al. 1990) toward the

¹ Operated by the University of California at Berkeley, the University of Illinois, and the University of Maryland, with support from the National Science Foundation.

TABLE 1
A STARLESS CORE IN TAURUS MOLECULAR CLOUD

Molecule	Transition	ν (MHz)	Beam Size (arcsec)	Field of View (arcsec)	Velocity Resolution (km s ⁻¹)
CCS.....	$J_N = 3_2-2_1$	33751.374 ^a	17.9 × 16.8	300	0.054
N ₂ H ⁺	$J F_1 F = 1 0 1-0 1 2$	93176.2650 ^b	19.9 × 16.4	108	0.039

^a Yamamoto et al. 1990.

^b Cazzoli et al. 1985.

center of the core using the Nobeyama 45 m telescope.² The single-dish observation was obtained in 1999. The beam size of the CCS observation is $\sim 52''$. The main-beam efficiency was $79\% \pm 3\%$. The 1024 channel FX spectrometer was used, with bandwidth 10 MHz and velocity resolution 0.087 km s^{-1} .

2.2. Submillimeter-Wave Observations

Submillimeter-wave dust continuum observations were obtained in 1997 October using the SCUBA (Submillimeter Common-User Bolometric Array; Holland et al. 1999) on the James Clerk Maxwell Telescope.³ Images, each approximately $2'$ across, were obtained at $850 \mu\text{m}$. The pointing was checked approximately hourly on a nearby source with known coordinates (CRL 618). The atmospheric opacity was monitored with a tipping radiometer operating at 225 GHz and was found to be very stable and highly transparent, with

² Nobeyama Radio Observatory is a branch of the National Astronomical Observatory, operated by the Ministry of Education, Science, Sports, and Culture.

³ The James Clerk Maxwell Telescope is operated by the Joint Astronomy Centre on behalf of the Particle Physics and Astronomy Research Council of the United Kingdom, the Netherlands Organization for Scientific Research, and the National Research Council of Canada.

values ranging from 0.05 to 0.06 at 1 mm wavelength (~ 0.2 at $850 \mu\text{m}$). The data were calibrated to Jy beam^{-1} by observing Uranus using the same observation configuration. The data were reduced and images combined using the ORACDR pipeline facility within the SURF data reduction package (Jenness & Lightfoot 1998; Jenness & Economou 1999). The beam size at $850 \mu\text{m}$ is $\sim 14''$.

3. RESULTS

3.1. Physical Properties of the Dense Core: Dust Distributions and Clumpy Structures

3.1.1. Overall Distribution of CCS and N₂H⁺ Molecules and Dust Continuum

A contour plot of the $850 \mu\text{m}$ dust continuum map is shown in Figure 1. Contour levels are indicated in the figure caption. Figure 2 shows the total intensity maps of CCS and N₂H⁺, summed up over twice the Gaussian dispersion of the lines, namely, within $6.00\text{--}6.76 \text{ km s}^{-1}$ for CCS and $5.92\text{--}7.06 \text{ km s}^{-1}$ for N₂H⁺ in V_{LSR} . The field center of both molecular line maps corresponds to the $850 \mu\text{m}$ dust peak position, i.e., $\alpha = 4^{\text{h}}28^{\text{m}}39^{\text{s}}.27$, $\delta = 26^{\circ}51'39''.0$ (J2000.0). Here we use 140 pc (Elias 1978) as a distance of the core. One can clearly see that interferometric images show more structures than the

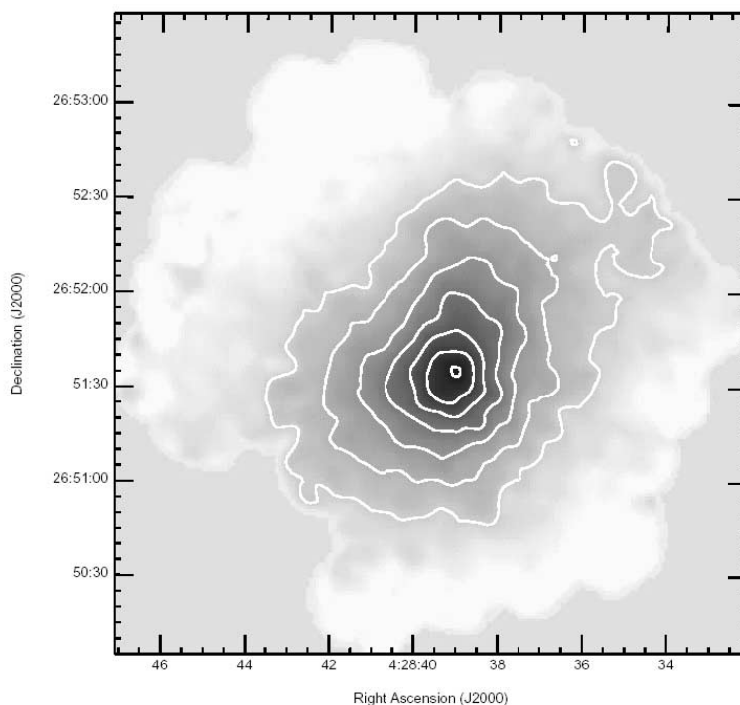


FIG. 1.—Total intensity map of $850 \mu\text{m}$ dust continuum of the starless core. The contours start at 2σ , which corresponds to 50 mJy beam^{-1} , with intervals of 2σ .

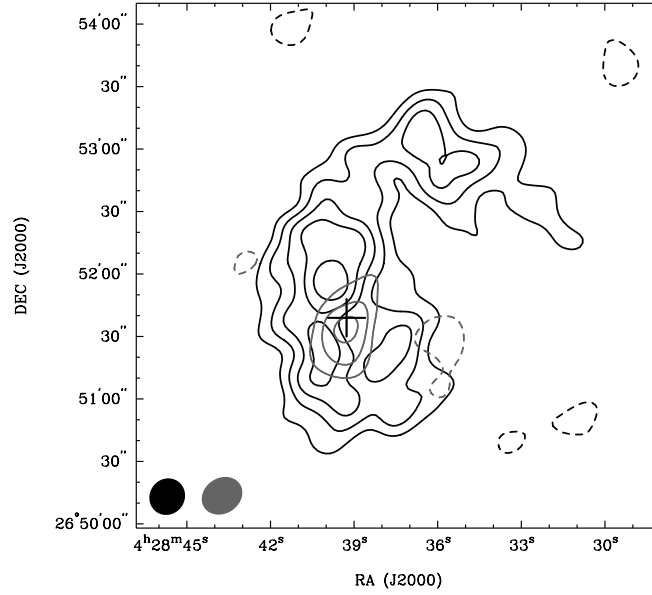


FIG. 2.—Total intensity map of the CCS $J_N = 3_2-2_1$ (black contour) and N_2H^+ (J, F_1, F) = (1 0 1-0 1 2) (gray contour) lines. The beam sizes for each map are shown in the left corner with the same colors of the contours. The contour spacing is 1.5σ , starting at $\pm 3 \sigma$ with $1.5 \sigma = 105 \text{ mJy beam}^{-1}$, for CCS and 1.5σ , starting at $\pm 3 \sigma$ with $1.5 \sigma = 255 \text{ mJy beam}^{-1}$, for N_2H^+ . Negative contours are drawn by dashed lines. The cross represents the field center of both maps.

the single-dish submillimeter continuum map. The CCS component has an elongated distribution in the northwest-southeast direction, similar to that of the $H^{13}CO^+ J = 1-0$ (Mizuno et al. 1994) and the $NH_3 (1, 1)$ map (Codella et al. 1997), with a similar size ($\sim 3' \times 2'$, i.e., $\sim 0.12 \times 0.08 \text{ pc}$ at 3σ level in brightness). The $850 \mu\text{m}$ dust continuum map also shows a similar elongation in the same direction. In the interferometric CCS map, one can see two major components, namely, a brighter component with a $\geq 9 \sigma$ peak in the south and a smaller northern component that has a 6σ peak. The southern component extends $\sim 120'' \times 60''$ ($\sim 0.08 \text{ pc} \times 0.04 \text{ pc}$) in the north-south direction. The northern component has a dimension of $\sim 60'' \times 30''$ ($\sim 0.04 \text{ pc} \times 0.02 \text{ pc}$) at FWHM, elongated northeast-southwest direction. Although the dust map does not cover all the area of the northern component, there is no obvious extended feature in the direction of the northern component. This may imply that this northern component is in a younger phase compared with the southern one. On the other hand, the N_2H^+ distribution is compact. The FWHM size of the N_2H^+ component has $\sim 50'' \times 30''$. Compared to the peak position of the $850 \mu\text{m}$ dust continuum, the center of N_2H^+ is $\sim 4''$ apart in the southern direction. These peak positions are within their pointing error range. The CCS distribution is more extended than the dust distribution.

In order to assess the difference of the radial distribution traced by each molecule, an ellipse centered at the N_2H^+ core was fitted to the N_2H^+ total intensity map. The averaged flux density was calculated in each elliptical annuli of $10''$ width in the two dimensions of the CCS and N_2H^+ total intensity maps. Figure 3 shows the resultant radial brightness distribution of each molecular component. The average radial profile of the dust continuum is also shown in the same diagram. The profiles of dust and N_2H^+ are quite similar, suggesting that N_2H^+ traces the core well, including the center. For CCS, the radial profile is quite different from the dust profile. CCS well traces an extended envelope component, rather than the core center. Clearly, the CCS has a weak peak at a radius of $\sim 20''-25''$ ($\sim 3000 \text{ AU}$) from the center. This is due to the three extended

peaks at a similar distance of $\sim 20''-25''$ from the core center. The dip at the core center may be caused either by (1) the existence of some extended structures larger than $4/3$ in size (see § 2.1) or by (2) an abundance decrease of the molecule at the center due to depletion and chemical reactions. Possibility 1, however, would be unlikely because (a) the measured missing flux of CCS, which is described in § 3.1.2, is not significant, and (b) typical patterns of such a tendency are not found in the channel maps, shown in § 3.1.5. One would be able to confirm it by making single-dish mapping observations of these transitions of the molecule.

3.1.2. Physical Properties toward the Core Center

To derive the optical depth, CCS and the isotope $CC^{34}S$ $J_N = 3_2-2_1$ lines have been observed toward the dust peak position, i.e., the core center. Figure 4 shows the spectra taken with the Nobeyama 45 m telescope. The optical depth τ of the molecular lines, τ_{CCS} and $\tau_{\text{CC}^{34}\text{S}}$, can be estimated from the ratio of the observed brightness temperatures of these transitions using

$$\frac{T_B[\text{CCS}]}{T_B[\text{CC}^{34}\text{S}]} = \frac{J_{\text{CCS}}(T_{\text{EX}}) - J_{\text{CCS}}(T_{\text{bg}})}{J_{\text{CC}^{34}\text{S}}(T_{\text{EX}}) - J_{\text{CC}^{34}\text{S}}(T_{\text{bg}})} \frac{1 - \exp(-\tau_{\text{CCS}})}{1 - \exp(-\tau_{\text{CC}^{34}\text{S}})}, \quad (1)$$

where

$$J(T) = \frac{h\nu/k}{\exp(h\nu/kT) - 1},$$

T_B is the brightness temperature, T_{EX} is the excitation temperature, T_{bg} is the cosmic background radiation temperature, h is the Planck's constant, ν is the center frequency of a molecular transition, and k is the Boltzmann constant. Assuming an excitation temperature of 10 K, which is a typical value for dark cloud cores, and a solar abundance ratio

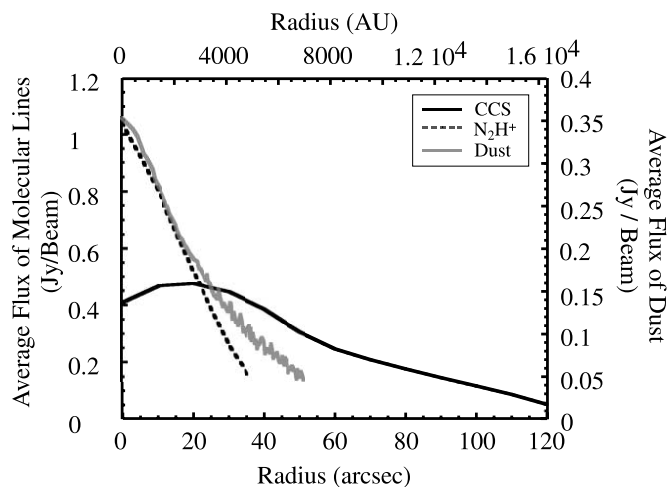


FIG. 3.—Average radial profile of CCS (solid line), N_2H^+ (dashed line), and the dust continuum (gray line) flux.

of $[^{32}S]/[^{34}S] = 23$, τ_{CCS} is estimated to be 0.87. This is an upper limit due to the poor signal-to-noise ratio of the $CC^{34}S$ line. The observed FWHM line width taken with the single-dish telescope is $0.33 \pm 0.02 \text{ km s}^{-1}$.

Figure 5 displays the N_2H^+ spectrum at $\alpha = 4^h28^m39^s.76$, $\delta = 26^\circ51'35''.1$ (J2000.0) taken with the Haystack 37 m telescope (Lee et al. 1999). The beam size is $27''$, and the main-beam efficiency is $18\% \pm 3\%$. Fitting the N_2H^+ spectrum, the excitation temperature and optical depth can be estimated by the following equations under the LTE condition:

$$T_B = [J(T_{EX}) - J(T_{bg})] \{1 - \exp[-\tau(v)]\} + \xi, \quad (2)$$

where

$$\tau(v) = \tau_{\text{total}} \sum_{m=1}^j C_m \exp \left[\frac{-(v - v_0 + v_m)^2}{2\sigma_{v_{\text{obs}}}^2} \right],$$

$$\sigma_{v_{\text{obs}}}^2 = \frac{\Delta v_{\text{FWHM}_{\text{obs}}}^2}{8 \ln 2}.$$

In these equations, $\tau(v)$ is the optical depth at the observed velocity v , ξ is the baseline error, τ_{total} is the total optical depth of all the hyperfine components, m stands for the m th hyperfine component, C_m is the normalized relative intensities of each hyperfine component, v is the LSR velocity, v_0 is the center LSR velocity of the cloud, v_m is the velocity difference from the standard velocity of different components, $\sigma_{v_{\text{obs}}}$ is the velocity dispersion of the observed line, and $\Delta v_{\text{FWHM}_{\text{obs}}}$ is the intrinsic FWHM observed line width. The value of j is 7 for the transition that we observed. We used the parameters of the molecule measured in laboratory (Cazzoli et al. 1985). By fitting equation (2) to the spectrum, the excitation temperature of the N_2H^+ component is estimated to be $5.0 \pm 0.2 \text{ K}$. For the isolated component, $JF_1F = 101-012$ at 93.176310 GHz (Cazzoli et al. 1985), which is used for our kinematic analysis, the optical depth is estimated to be 1.2 ± 0.1 . The measured τ_{total} was 11 ± 1.3 . The $\Delta v_{\text{FWHM}_{\text{obs}}}$ of N_2H^+ with the single-dish telescope is $0.38 \pm 0.09 \text{ km s}^{-1}$.

In order to estimate the missing flux, the spectra taken with the single-dish telescopes and the interferometer are compared. Figure 6 shows the spectra of both molecular transitions. For

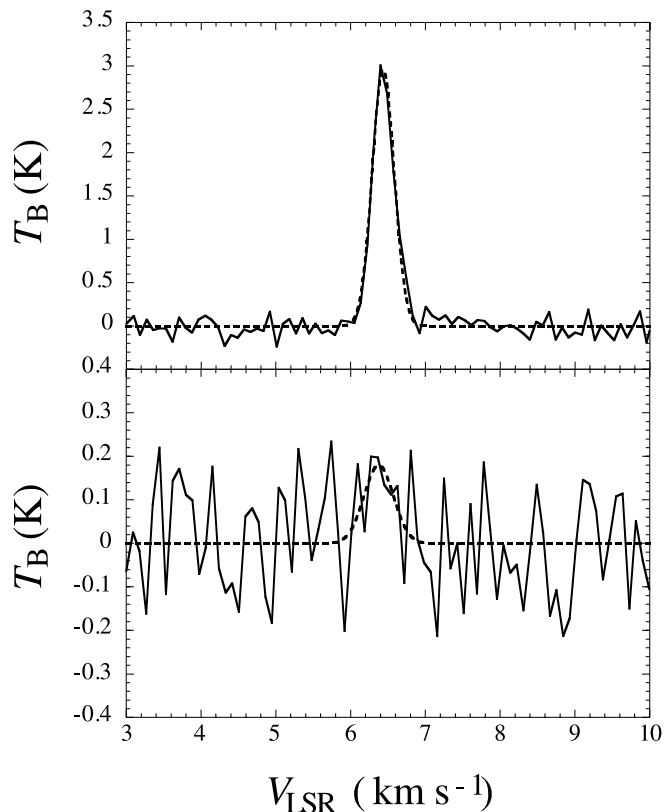


FIG. 4.—Spectra of $J_N = 3_2 - 2_1$ transition of CCS and the isotope $CC^{34}S$, taken with the Nobeyama 45 m telescope toward the dust continuum peak. The dotted lines indicates the Gaussian fitting of the spectra.

each line, the spectra were measured at the same position. In addition, the spectra obtained with the interferometer were convolved with the same beam sizes as those of corresponding single-dish observations. The missing flux is estimated from $[1 - (I_i/I_s)]$, where I_i and I_s are integrated intensity of the spectra taken with interferometer and the single-dish telescope, respectively. The missing fluxes of CCS and N_2H^+ were estimated to be $15\% \pm 4\%$ and $56\% \pm 4\%$, respectively. Thanks to the short antenna spacings and the large primary beam of the CCS observations at the long wavelength of the

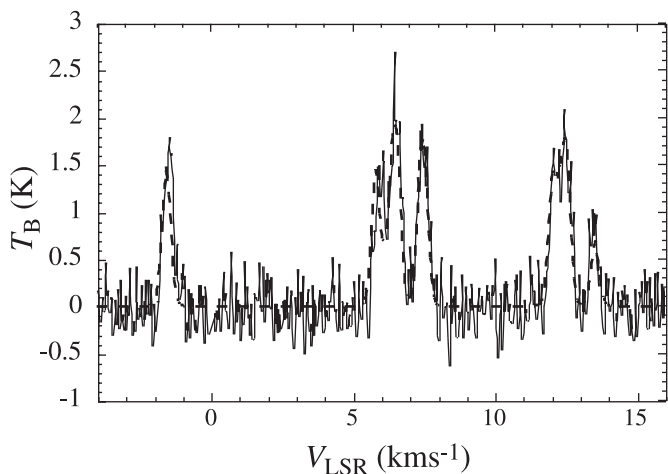


FIG. 5.—Spectrum of $J = 1-0$ transition of N_2H^+ at $\alpha = 4^h28^m39^s.76$, $\delta = 26^\circ51'35''.1$ (J2000.0) taken with the Haystack 37 m telescope. The dashed line shows the Gaussian fitting.

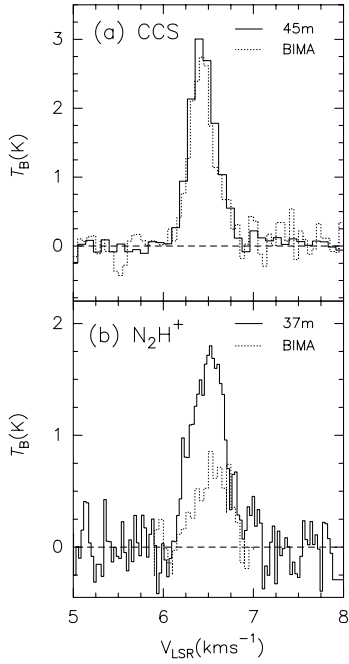


FIG. 6.—Comparison of the spectra of the molecular transitions (a) for CCS and (b) for N_2H^+ measured with the single-dish telescopes (the Nobeyama 45 m telescope for CCS and the Haystack 37 m telescope for N_2H^+ ; *solid lines*) and the interferometer (*dotted lines*). The spectra taken with the interferometer are corrected for the difference in the solid angles between each measurement.

transition, its missing flux is relatively small. Note that these missing flux values for each molecular observation are good only toward the central $52''$ (i.e., the beam of the single-dish observations) direction with the same beam size. Missing flux at each position depends on the spatial frequency (i.e., the structure) of the core traced by the molecules.

3.1.3. Deriving Masses

Assuming LTE, we can derive masses of the cores and clumps traced by the molecular lines. For molecular spectra of rotational transitions, the following equation is valid under the LTE condition:

$$T_B = \frac{8\pi^3}{3hc} \frac{\nu}{\Delta\nu} S_{J+1,J} \mu^2 \left(\frac{n_J}{g_J} - \frac{n_{J+1}}{g_{J+1}} \right) L, \quad (3)$$

where c is the speed of light, $\Delta\nu$ is the line width in frequency, $S_{J+1,J}$ is the transition strength for the rotational transition of $J+1 \rightarrow J$, μ is the dipole moment of the molecule, n_J and g_J are the number of particles and the degeneracy ($=2J+1$) at the transition level J , and L is the path length of a molecular dense clump. The following equations are defined by the LTE condition:

$$\frac{n_{J+1}}{n_J} = \frac{g_{J+1}}{g_J} \exp\left(-\frac{\Delta E}{kT_{EX}}\right), \quad (4)$$

$$n_J = \frac{ng_J}{Q} \exp\left(-\frac{E_J}{kT_{EX}}\right), \quad (5)$$

where ΔE is the energy difference between the transitions ($=h\nu$), n is the total number density of the molecule, E_J is the

energy of the J level, and Q is the partition function described by

$$Q = \sum_{J=0}^{\infty} g_J \exp\left(-\frac{E_J}{kT_{EX}}\right). \quad (6)$$

Using equations (4)–(6), equation (3) can be modified in order to derive the column density N of the molecule as follows:

$$N = \int_0^L n ds = \frac{3h}{8\pi^3} \frac{Q}{S_{J+1,J} \mu^2} \exp\left(\frac{E_J}{kT_{EX}}\right) \times \frac{1}{1 - \exp(-h\nu/kT_{EX})} \frac{\tau}{1 - \exp(-\tau)} \int_v T_B dv. \quad (7)$$

For CCS, μ and $S_{J+1,J}$ are 2.8 (Murakami 1990) and 2.976D (Yamamoto et al. 1990), respectively, for the $J_N = 3_2-2_1$ transition. The column density of molecular hydrogen is estimated by using

$$N(H_2) = \frac{N}{X}, \quad (8)$$

where X is the abundance ratio of the molecule to molecular hydrogen (X is estimated in § 3.1.4). To estimate the LTE masses of clumps, M_{LTE} at a distance of 140 pc, we use

$$\frac{M_{LTE}}{M_{\odot}} \sim 5.163 \times 10^{-31} \frac{l_{maj} l_{min}}{\text{arcsec}^2} \frac{d^2}{\text{pc}^2} \frac{N(H_2)}{\text{cm}^{-2}}, \quad (9)$$

where l_{maj} and l_{min} are the FWHM dimensions of the major and minor axes in arcseconds, d is the distance in parsecs, and N is column density in cm^{-2} . From the observed velocity dispersion of the spectra, the virial masses of the clumps, M_{VIR} , with a density distributions of $\rho \propto R^{-e}$ (ρ is the density, R is the radius, and e is an integer, $0 \leq e \leq 2$) can be estimated using

$$M_{VIR} = \frac{(5-2e)R}{(3-e)G} \sigma_{v_{total}}^2, \quad (10)$$

where G is the gravitational constant and $\sigma_{v_{total}}$ is the full turbulent velocity dispersion, including thermal and non-thermal components, in three dimensions averaged over the whole system for a clump. Note that the virial mass above is calculated without considering the external pressure because it is not easy to estimate it and also because it would be negligible when the temperature is similar over the core or cooler at the outer regions of the core. If the external pressure is not negligible, then the clumps not virialized could be still confined. We can describe $\sigma_{v_{total}}$ as

$$\sigma_{v_{total}} = \sqrt{\sigma_{v_{obs}}^2 + kT_K \left(\frac{1}{m_{H_2+He}} - \frac{1}{m_{obs}} \right)}, \quad (11)$$

where T_K is the kinetic temperature, m_{H_2+He} is the average mass unit ($=2.33$ amu), and m_{obs} is the mass of the observed

molecule; m_{obs} for CCS and N_2H^+ is 56 and 29 amu, respectively. The virial masses for the different density distributions of uniform (model 1), $\rho \propto R^{-1}$ (model 2), and $\propto R^{-2}$ (model 3) are estimated according to equation (10). To calculate the virial masses of the clumps, R is considered to be $(l_{\text{maj}}/l_{\text{min}})^{1/2}$ in this paper.

3.1.4. Abundances of the Molecules

Molecular abundances can be estimated from a comparison between the LTE column density of the molecule and the gas and dust column density. To estimate the gas and dust mass, $M_{\text{gas+dust}}$, we use

$$M_{\text{gas+dust}} = \frac{F_\nu d^2}{\kappa_\nu B_\nu(T_d)}, \quad (12)$$

where κ_ν is the mass absorption coefficient by dust grain, B_ν is the Planck function, F_ν is the flux density of the continuum emission at frequency ν , and T_d is the dust temperature. The dust temperature is assumed to be 10 K, and the gas-to-dust ratio is assumed to be 100. The flux density of 850 μm toward the core center is measured to be 0.35 Jy beam $^{-1}$. Here the opacity per gram of gas and dust at frequency, $\kappa_{\nu 352.7 \text{ GHz} (= \lambda 850 \mu\text{m})}$, is assumed to be $2 \times 10^{-2} \text{ cm}^2 \text{ g}^{-1}$ (Shirley et al. 2000). This κ_ν is obtained by a model for thin ice mantles (Ossenkopf & Henning 1994). Toward the core center, the abundances X of these molecules were estimated to be $(8 \pm 3) \times 10^{-9}$ for CCS and $(7 \pm 3) \times 10^{-9}$ for N_2H^+ , respectively. One should keep in mind that these values would be upper limits because there is missing flux for both observations (see § 3.1.2). However, these X values are in the same range as the values previously investigated toward other dense cores by several authors (Langer et al. 1995; Peng et al. 1998; Benson, Caselli, & Myers 1998; Dickens et al. 2000). For simplicity, the abundances are assumed to be constant over the core to estimate densities and masses in this paper. Although the abundance of CCS is most likely decreased at the core center (see § 3.1.1), it is hard to estimate the abundances except at the core center because the dust continuum is not detected in the outer region of the core. Accordingly, the X of CCS estimated toward the core center is used as a representative value in this paper.

One can estimate the mass of the core from equation (12). The total flux density of the dust continuum at 850 μm is 4.72 ± 0.05 Jy. Under the same assumptions described above, the estimated mass of the core is $1.51 \pm 0.02 M_\odot$.

3.1.5. Clumpy Structures inside the Core

Figures 7 and 8 show the channel maps of CCS and N_2H^+ , respectively. Both maps clearly reveal clumpy structures inside the core.

To identify clumps, an automatic and objective routine (Williams, de Gueuss, & Blitz 1994) is used. The peak of each clump is required to be detected above the 4σ level. The contrast (ΔT) of each clump, which is one of the input parameters in the program, is set to be $2 \times T_{\text{rms}}$ to avoid a high percentage of false detections. This condition gives us an expected rate of false detection $\lesssim 2\%$ (Williams & Teuben 1997). In Figures 7 and 8 the clumps are labeled C1, C2, and so forth for the CCS and N1, N2, and so on for the N_2H^+ clumps, respectively. The dotted line in Figure 8 represents the interferometer primary-beam half-power for the molecular line observation. The primary-beam FWHP of the CCS observation

is mostly out of the diagram (see Table 1). Figures 9 and 10 show the spectra of each clump. The spectra are made by considering regions brighter than 3σ level on the integrated intensity maps of each clump. When there are multiple components along a given direction toward a clump, the spectra are fitted by multivelocity components. The dotted lines indicate Gaussian fittings for the components.

The parameters for each clump are cataloged in Tables 2 and 3 for CCS and N_2H^+ , respectively. The masses of each clump are derived using the equations described in § 3.1.3. For the CCS clump C6, the mass cannot be estimated because of the contamination by other extended components surrounding the clump. Note that the observed FWHM velocity widths in the tables are the values after the instrumental broadening effect have been subtracted. The abundances of the molecules derived in § 3.1.4 are used to derive the LTE mass. The listed LTE masses in Tables 2 and 3 are lower limits because of unknown missing flux for every clump, as described in § 3.1.2. There are no clumps that coincide in both molecular images in both position and velocity. That would most likely be because these molecular lines trace different regions; namely, N_2H^+ traces the denser core center region where CCS does not trace, as described in § 3.1.1. Further discussion of this issue will be found in § 4.1.

The average radius of the CCS clumps is 3.3×10^{-2} pc (~ 6600 AU), slightly larger than the average radius of the N_2H^+ clumps of 2.1×10^{-2} pc (~ 4200 AU). The average FWHM velocity width of the CCS clumps, 0.21 km s^{-1} , is also larger than that of the N_2H^+ clumps, 0.17 km s^{-1} . The average LTE mass of the N_2H^+ clumps, $0.072 M_\odot$, is much smaller than that of the CCS clumps, $0.24 M_\odot$, which may be due to significant missing flux in the N_2H^+ data. If we assume the missing flux of 15% for CCS and 56% for the N_2H^+ , the average mass of CCS and N_2H^+ would be 0.28 and $0.17 M_\odot$, respectively.

The comparison between the LTE mass and the virial mass enables us to infer gravitational stability for each clump. In Tables 2 and 3, three cases of virial masses calculated by the mass distributions are listed. One must be aware that the LTE mass would be a lower limit because of the missing flux effect, as described in the previous paragraph. If one assumes that a clump with LTE mass $M_{\text{LTE}} \gtrsim \frac{1}{2} M_{\text{VIR}}$ in model 1 (constant density distribution; see § 3.1.3) is bound, CCS clump C1 and N_2H^+ clump N1 may be gravitationally bound. If one uses the criterion that a structure has mass $M_{\text{LTE}} \gtrsim \frac{1}{2} M_{\text{VIR}}$ in model 3 ($\rho \propto R^{-2}$) for virialization, then all the CCS clumps except for C8 and the N_2H^+ clumps N1 and N3 are virialized. Model 2 is between models 1 and 3. The detailed kinetic structure there is described in § 3.2. In the spectrum of N3, one can see a negative feature centered at $V_{\text{LSR}} \sim 6.43 \text{ km s}^{-1}$. This is because there is an offset between the position of N3 and the N_2H^+ center peak. Imaging procedures can produce this kind of dip because of a strong component at the core center. N4 is an extreme case among the clumps identified here in terms of the velocity dispersion. This clump in the channel map has a 5σ peak in brightness with a typical size of the clumps and has extremely narrow velocity dispersion. This narrow line width is most likely much narrower than the actual line width, mainly because of the low signal-to-noise ratio. However, the probability that this clump is not real is only $\sim 0.01\%$, derived by a simple statistics estimation to have 5σ peak in one of the 30 channel maps. One cannot tell whether N4 is virialized or not because it is hard to estimate the real line width. N4 is excluded from the detailed analysis of the clumps,

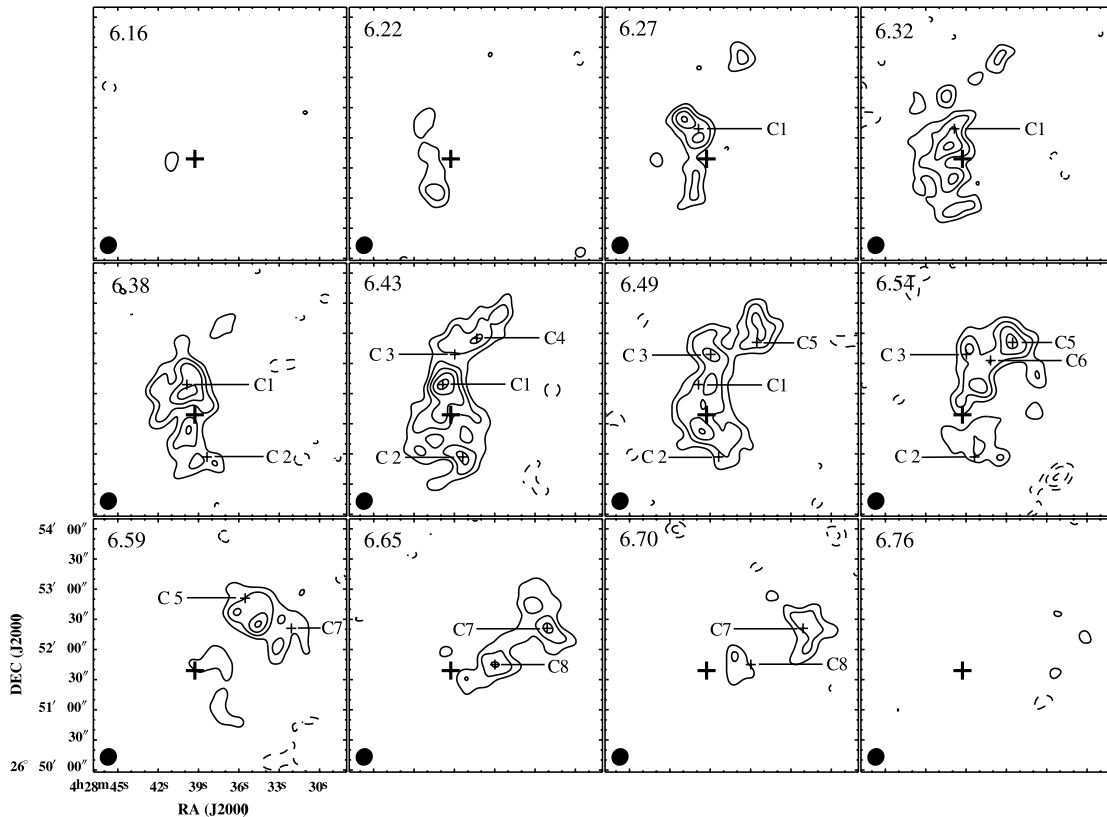


FIG. 7.—Channel map of the CCS line. The contour spacing is $\pm 1.5 \sigma$, starting at $\pm 3 \sigma$ with $510 \text{ mJy beam}^{-1}$. The V_{LSR} for each panel is given in the upper left-hand corner. The heavy cross represents the field center, same as Fig. 2.

described in § 4, because of the difficulty of estimating the real line width.

3.2. Kinetic Structure Inside the Core

To infer the kinetic structure within the core, position-velocity diagrams are made for the CCS and N_2H^+ components. Fitting an elliptical Gaussian to the total intensity map of the N_2H^+ component, the major and minor axes have been determined, as shown in Figure 11a.

Figure 11b shows the position-velocity diagrams of the molecular lines along the major axis. The CCS northern component, which is located at offsets $\sim -60''$ to $-130''$ in the diagram in Figure 11b, coincides with no N_2H^+ components, because of lack of sensitivity of the N_2H^+ data in the area (see Fig. 8). The CCS position-velocity structure in the diagram shows some interesting characteristics worthy of note. First of all, the CCS components are distributed along half of a ring in the diagram. Secondly, the half-ring center is located at $\sim -30''$ from the dust center, which is located at 0 in position in the diagram in Figure 11b. The dust center should be identical to the dynamical center. A ring shaped position-velocity structure traced by the same molecular transition is found in L1544 (Ohashi et al. 1999) and can be explained by simultaneous infall and rotation. If the half-ring structure of CCS of this core can also be explained by rotation and infall, as shown in the L1544 case, the center of the rotation and infall, i.e., the dynamical center of the system, must be located at the dust center. However, the observational results show that these positions are different in the L1521F case. The difference of the centers may suggest that either (1) there is some extended large-scale structure, which is not detected with the interferometric observations and would be

significant in determining the dynamical center, or (2) the CCS northern component has a different dynamical center from the southern one, so that one should consider only the components located within $\sim 60''$ for the southern component. The possibility of (1) would be low because the reasons described in § 3.1.1.

On the other hand, in the same diagram (Fig. 11b), there are four major N_2H^+ components. The main N_2H^+ component in Figure 11b is the one closest to the center. It traces part of the clump N2. It is distributed along a line in the diagram and has quite a different elongation from that of CCS in the diagram. Three of the four N_2H^+ components coincide with the positions of the CCS components. Two of the four N_2H^+ components, which are at $\sim 20''$ and $\sim 35''$ in the position, are located at two of the CCS peaks in the diagram. It would be most likely that they trace the same physical entities. One of the N_2H^+ components that does not have any counterpart in the CCS components is located along the line of the main N_2H^+ component, N2. This traces part of the N_2H^+ clump, N4. The line connecting N2 and N4 is elongated almost perpendicularly to the tangent line of the ring of the CCS component. This means that the velocity gradient of the N_2H^+ component is not in the same sense as that of the CCS component. We discuss these velocity gradients in § 4.2.

Figure 11c shows the position-velocity diagram of these molecules along the minor axis. One can see two N_2H^+ components in the diagram. These trace part of the N_2H^+ clumps of N2 and N4. These two components are separated from each other by 0.16 km s^{-1} . The prominent CCS component in the diagram is part of the biggest CCS clump, C1. There is almost no correlation between CCS and N_2H^+ components in the diagram.

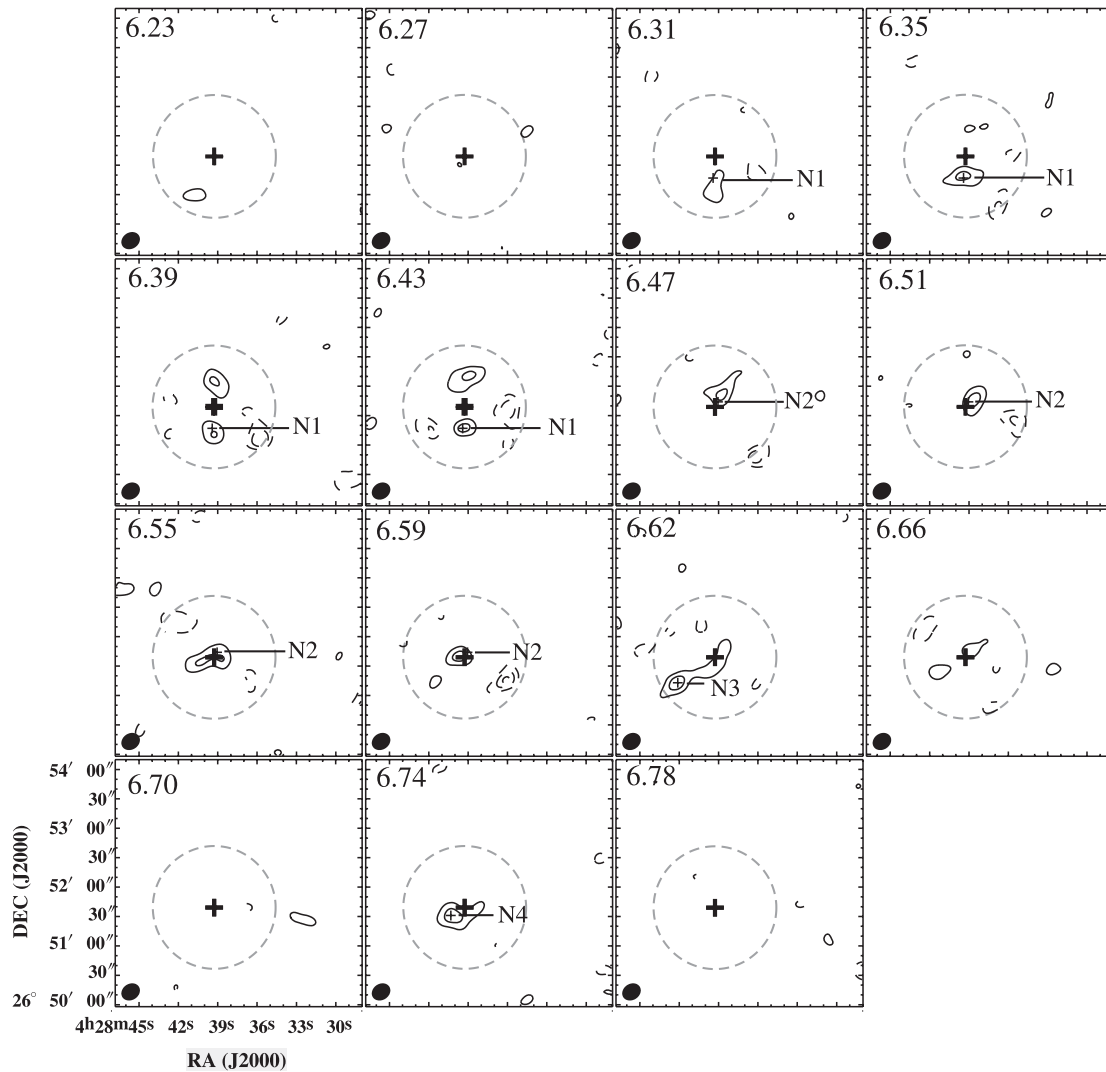


FIG. 8.—Channel map of the N_2H^+ line. The annotation is the same as in Fig. 7. The contour spacing is $\pm 1.5 \sigma$, starting at $\pm 3 \sigma$ with $2.16 \text{ Jy beam}^{-1}$. The heavy cross marks the field center, same as Fig. 2. The map area is the same as Fig. 7 for comparison. The dashed gray line represents the interferometer primary-beam half-power point.

In order to delineate the overall velocity structure, the velocity maps of CCS and N_2H^+ are shown in Figures 12 and 13, respectively. The CCS has a global velocity gradient from east to west. On the other hand, N_2H^+ does not have a global gradient. This is consistent with the result shown in Figure 11*b*. At the N_2H^+ core center, a systematic velocity gradient is found from west to east, which is in the opposite sense to the global velocity gradient of CCS. This systematic velocity gradient is observed in the clumps N2 and N4. Assuming that the velocity gradients are explained by rotation, the observational results indicate that the rotation of the outer envelope (size $\sim 0.08 \text{ pc}$) and that of the central compact region (size $\sim 0.03 \text{ pc}$) have different axes with almost opposite sense of rotation. This clearly means that N_2H^+ is dynamically independent from the major CCS components.

This kind of velocity gradient has never before been recognized toward any dense cores and clumps. For example, for L1544, both CCS (Ohashi et al. 1999) and N_2H^+ (Williams et al. 1999) imaging show the velocity gradients with the same direction. This issue will be discussed further in § 4.3. A possible model which may explain the multiple kinetic structure will be described elsewhere. Clump N2, which has

a scale of $\sim 4900 \text{ AU} \times 3900 \text{ AU}$ and is located at the dust center, might evolve into a protostar in the future.

4. DISCUSSION

4.1. Line Width–Size Correlation of Starless Dense Cores and Clumps

Clumpy structures are found inside the core by imaging with the CCS and N_2H^+ transitions. Although there are no clumps obviously detected in the dust map (Fig. 1), these clumpy structures would reflect real physical entities for the following reasons. First of all, synthesis imaging is more sensitive to clumpy structures than single-dish mapping because extended structures are resolved out with synthesis imaging (see also § 2.1). Second, the dust continuum map shows only the mass distribution integrated along the line of sight, without any velocity information, while N_2H^+ and CCS maps have velocity information, so that one can distinguish components located along the same line of sight but having different velocities. In fact, the clumpy structures are identified on channel maps of N_2H^+ and CCS.

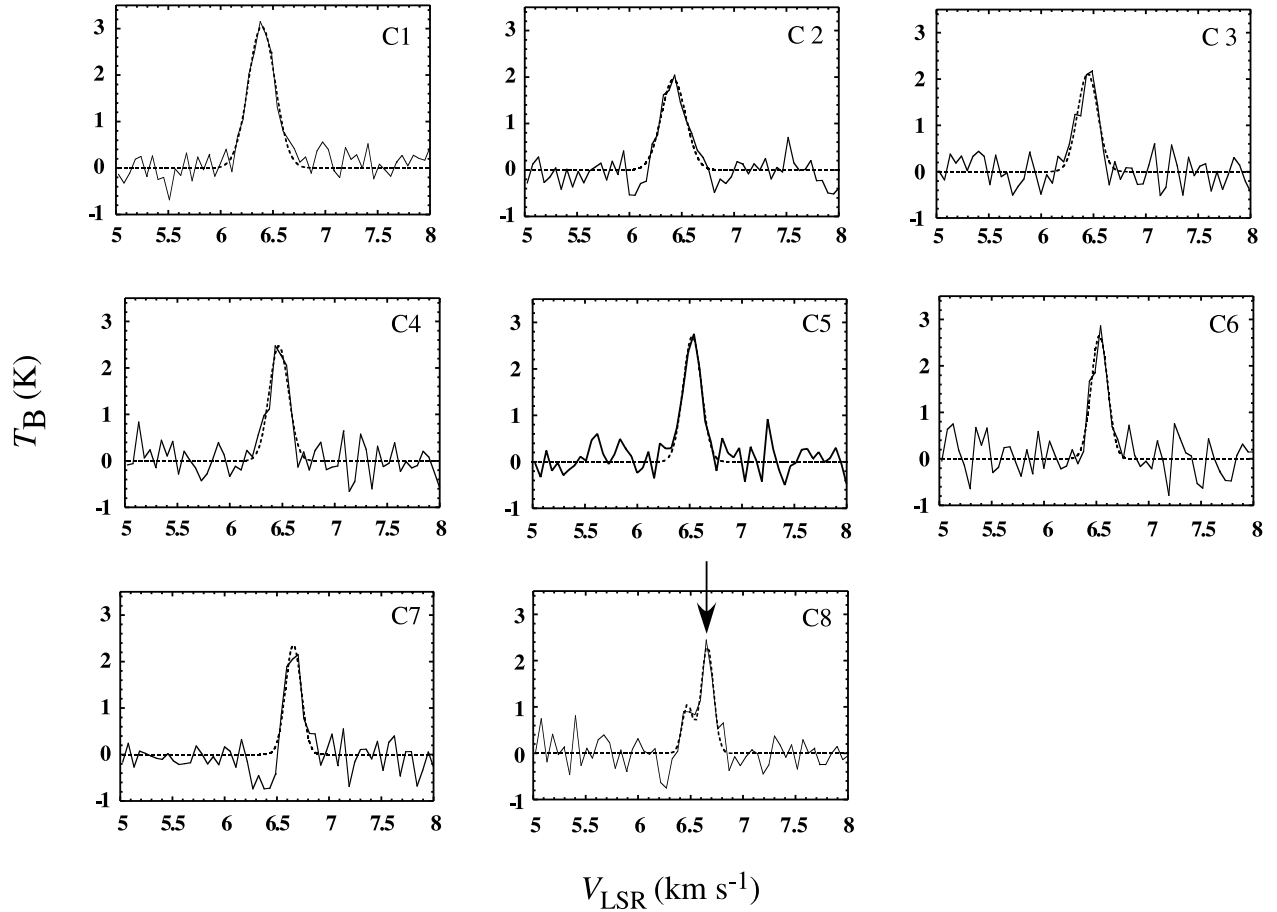


FIG. 9.—Black lines show spectra of CCS for each clump, with dashed lines for the Gaussian fittings. An arrow is marked for the component of C8 to distinguish it from the other component detected along the same line of sight.

We note that there are no clumps detected in both N_2H^+ and CCS, even though we could expect clumps to be detected in both lines if they are real physical entities. We should note, however, that N_2H^+ and CCS mostly traces different areas of the core: N_2H^+ mainly traces the innermost of the core, while CCS traces the outer parts of the core (see Fig. 3). Hence, we cannot really expect each clump to be detected in both lines. Although there are two velocity components detected in both CCS and N_2H^+ , they are not identified as clumps, as shown in § 3.2.

In order to compare the physical and statistical properties of the clumps that are found in this work with other clumps and cores previously reported (Fuller & Myers 1992; Langer et al. 1995; Peng et al. 1998; Jijina, Myers, & Adams 1999), their line width–size correlations have been investigated. Here observations with C^{18}O , NH_3 , CCS, CS, and N_2H^+ toward several dense cores and clumps are included for comparison; m_{obs} for C^{18}O , NH_3 , and CS is taken to be 30, 17, and 44 amu, respectively. For the NH_3 cores (Jijina et al. 1999), only those with temperatures lower than 10 K are included.

Figure 14 shows the line width–size relations of the CCS and N_2H^+ clumps, plotted with previous results done by several authors for comparison. The nonthermal velocity dispersion $\sigma_{v_{\text{nt}}}$ is derived as

$$\sigma_{v_{\text{nt}}} = \sqrt{\sigma_{v_{\text{total}}}^2 - \frac{kT_K}{m_{\text{H}_2+\text{He}}}}. \quad (13)$$

The top plot shows the observed velocity dispersion $\sigma_{v_{\text{obs}}}$ -size relation. The middle is the turbulent velocity dispersion $\sigma_{v_{\text{total}}}$ -size relation. The bottom shows the nonthermal line width $\sigma_{v_{\text{nt}}}$ -size relation. These relations can be fitted by

$$\sigma_v = AR^P, \quad (14)$$

where σ_v is the velocity dispersion (in km s^{-1}) and R is size (radius) of a clump in parsecs. For the $\sigma_{v_{\text{obs}}}$ -size relation, P is 0.40 ± 0.04 and A is 0.29 ± 0.02 . These values are similar to those found by Peng et al. (1998) and Fuller & Myers (1992). For the $\sigma_{v_{\text{nt}}}$ -size relation, P is 0.45 ± 0.05 and A is 0.28 ± 0.03 . It is slightly shallower than the result 0.7 ± 0.1 reported by Fuller & Myers (1992) but steeper than the values reported by Barranco & Goodman (1998) and Goodman et al. (1998). Regarding the $\sigma_{v_{\text{total}}}$ -size relation, $P = 0.11 \pm 0.01$ and $A = 0.29 \pm 0.01$ are obtained. Compared with the other results (Larson 1981; Fuller & Myers 1992), this slope is obviously shallower than the value 0.38 reported by Larson (1981); however, it is closer to the slope 0.20 ± 0.04 obtained by Fuller & Myers (1992). Although the small number of clumps reported in this paper do not improve the statistics of the line width–size correlation significantly, they do extend the relation to much smaller clumps, and they basically follow the line width–size correlation slope. In any case, this indicates that some coherence mechanism that forms observed cores and clumps exists even to this small scale (order of 10^{-2} pc, i.e., 10^3 AU).

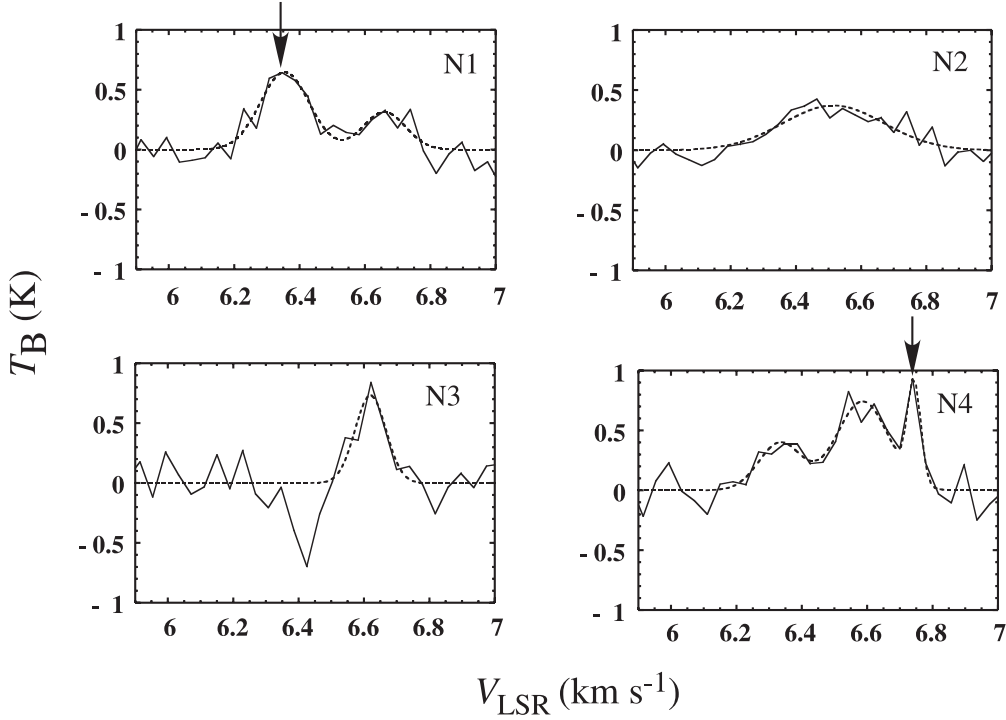


FIG. 10.—Spectra of the N_2H^+ clumps are shown in black lines. Each of them is fitted by a Gaussian, shown by dotted lines. The components of N1 and N4 are marked with an arrow for each to distinguish the clumps' components from the other components detected along the same line of sight.

If one assumes Kolmogorov turbulence diffusion (Kolmogorov 1941) for the dense cloud cores and clumps, the slope, P , for the $\sigma_{v_{\text{total}}}$ -size relation will be $\frac{1}{3}$ (Larson 1981). The slope obtained here for the total velocity dispersion is smaller than that of Kolmogorov turbulence. From the virial theorem,

$$\sigma_{v_{\text{total}}} \propto R\sqrt{n}, \quad (15)$$

where n is the total number density of the gas per cm^3 . If we assume that the energy transformation rate from kinetic to

thermal energy per cm^3 ($\sim \sigma_{v_{\text{total}}}^3 R^{-1}$ in Kolmogorov's law), ϵ' , is also proportional to the number density (and assuming the relation works for compressible gas), the following equation can be written:

$$\epsilon' \propto \frac{n\sigma_{v_{\text{total}}}^3}{R}. \quad (16)$$

According to Kolmogorov's assumption, ϵ' is constant. Since both n in the equations (15) and (16) should be the same, P in

TABLE 2
CATALOG OF CCS CLUMPS

CLUMP	CENTER POSITION (J2000)		V_{LSR}^a (km s^{-1})	Size ^b (arcsec)	$\Delta v_{\text{FWHM}_{\text{obs}}}^{a,c}$ (km s^{-1})	$\int T_B dv^{a,d}$ (K km s^{-1})	$N(\text{CCS})^{a,e,f}$ (10^{13}cm^{-2})	M_{LTE}^a (M_{\odot})	$M_{\text{VIR}}(M_{\odot})$		
	α	δ							Model 1 ^g	Model 2 ^h	Model 3 ⁱ
C1.....	4 28 39.87	26 52 2.5	6.38(1)	72 × 51	0.28(2)	0.8(1)	3.0(3)	0.52(7)	0.92	0.86	0.55
C2.....	4 28 38.37	26 50 57.0	6.42(1)	61 × 32	0.27(3)	0.6(1)	2.0(3)	0.18(3)	0.60	0.54	0.36
C3.....	4 28 38.97	26 52 43.3	6.45(1)	42 × 40	0.22(3)	0.5(1)	1.8(3)	0.14(3)	0.55	0.50	0.33
C4.....	4 28 37.33	26 52 55.0	6.47(1)	60 × 38	0.21(2)	0.5(1)	2.0(3)	0.21(4)	0.56	0.51	0.34
C5.....	4 28 35.34	26 52 51.0	6.53(1)	53 × 48	0.21(2)	0.6(1)	2.0(3)	0.24(3)	0.63	0.57	0.38
C6.....	4 28 37.18	26 52 33.0	6.53(1)	...	0.18(2)	0.5(1)	1.8(3)
C7.....	4 28 32.00	26 52 23.9	6.66(1)	56 × 46	0.17(2)	0.4(1)	1.5(3)	0.18(4)	0.56	0.51	0.34
C8.....	4 28 35.98	26 51 45.0	6.66(1)	44 × 38	0.13(2)	0.3(1)	1.1(3)	0.09(2)	0.42	0.38	0.25

NOTE.—Units of right ascension are hours, minutes, and seconds, and units of declination are degrees, arcminutes, and arcseconds.

^a The numbers in parentheses represent one standard deviation in units of the last significant digit.

^b Major and minor axes of the FWHM clump area.

^c Instrumental effect is subtracted.

^d The integrated intensity.

^e It is derived by assuming the LTE condition with excitation temperature of 10 K.

^f CCS fractional abundance $\chi(\text{CCS})$ is 8.0×10^{-9} ; κ is set to be $2 \times 10^{-2} \text{ cm}^2 \text{ g}^{-1}$ with the condition of the dust temperature of 10 K.

^g Virial mass for uniform density distribution, assumed $T_K = 10$ K.

^h Virial mass for density distribution of the form $\rho \sim R^{-1}$, assumed $T_K = 10$ K.

ⁱ Virial mass for density distribution of the form $\rho \sim R^{-2}$, assumed $T_K = 10$ K.

TABLE 3
CATALOG OF N_2H^+ CLUMPS

CLUMP	CENTER POSITION (J2000)		$V_{\text{LSR}}^{\text{a,b}}$ (km s^{-1})	Size ^c (arcsec)	$\Delta v_{\text{FWHM}_{\text{obs}}}^{\text{a,d}}$ (km s^{-1})	$\int T_B dv^{\text{a,e}}$ (K km s^{-1})	$N(\text{N}_2\text{H}^+)^{\text{a,f}}$ (10^{12} cm^{-2})	$M_{\text{LTE}}^{\text{a,g}}$ (M_{\odot})	$M_{\text{VIR}} (M_{\odot})$		
	α	δ							Model 1 ^h	Model 2 ⁱ	Model 3 ^j
N1.....	4 28 39.17	26 51 39.0	6.35(1)	28 × 30	0.17(3)	0.12(2)	9(2)	0.11(3)	0.33	0.30	0.20
N2.....	4 28 39.06	26 51 43.8	6.52(2)	35 × 28	0.36(4)	0.14(2)	11(2)	0.16(1)	0.66	0.60	0.40
N3.....	4 28 42.11	26 51 13.0	6.62(1)	43 × 23	0.10(3)	0.08(3)	6(2)	0.09(4)	0.31	0.28	0.18
N4.....	4 28 40.32	26 51 31.0	6.74(1)	36 × 29	...	0.02(2)	2(1)	0.03(2)

NOTE.—Units of right ascension are hours, minutes, and seconds, and units of declination are degrees, arcminutes, and arcseconds.

^a The numbers in parentheses represent one standard deviation in units of the last significant digit.

^b To adjust the center velocity of the main component, $JF_1F = 1\ 2\ 3-0\ 1\ 2$ transition, 8.047 km s^{-1} is added to the actual velocity of the isolated component, $JF_1F = 101-012$ transition.

^c Major and minor axes of the FWHM clump area.

^d Instrumental effect is subtracted.

^e The integrated intensity.

^f It is derived by assuming the LTE condition with excitation temperature of 10 K.

^g N_2H^+ fractional abundance $X(\text{N}_2\text{H}^+)$ is 6.7×10^{-10} ; κ is set to be $2 \times 10^{-2} \text{ cm}^2 \text{ g}^{-1}$ with the condition of the dust temperature of 10 K.

^h Virial mass for uniform density distribution, assumed $T_K = 10 \text{ K}$.

ⁱ Virial mass for density distribution of the form: $\rho \sim R^{-1}$, assumed $T_K = 10 \text{ K}$.

^j Virial mass for density distribution of the form: $\rho \sim R^{-2}$, assumed $T_K = 10 \text{ K}$.

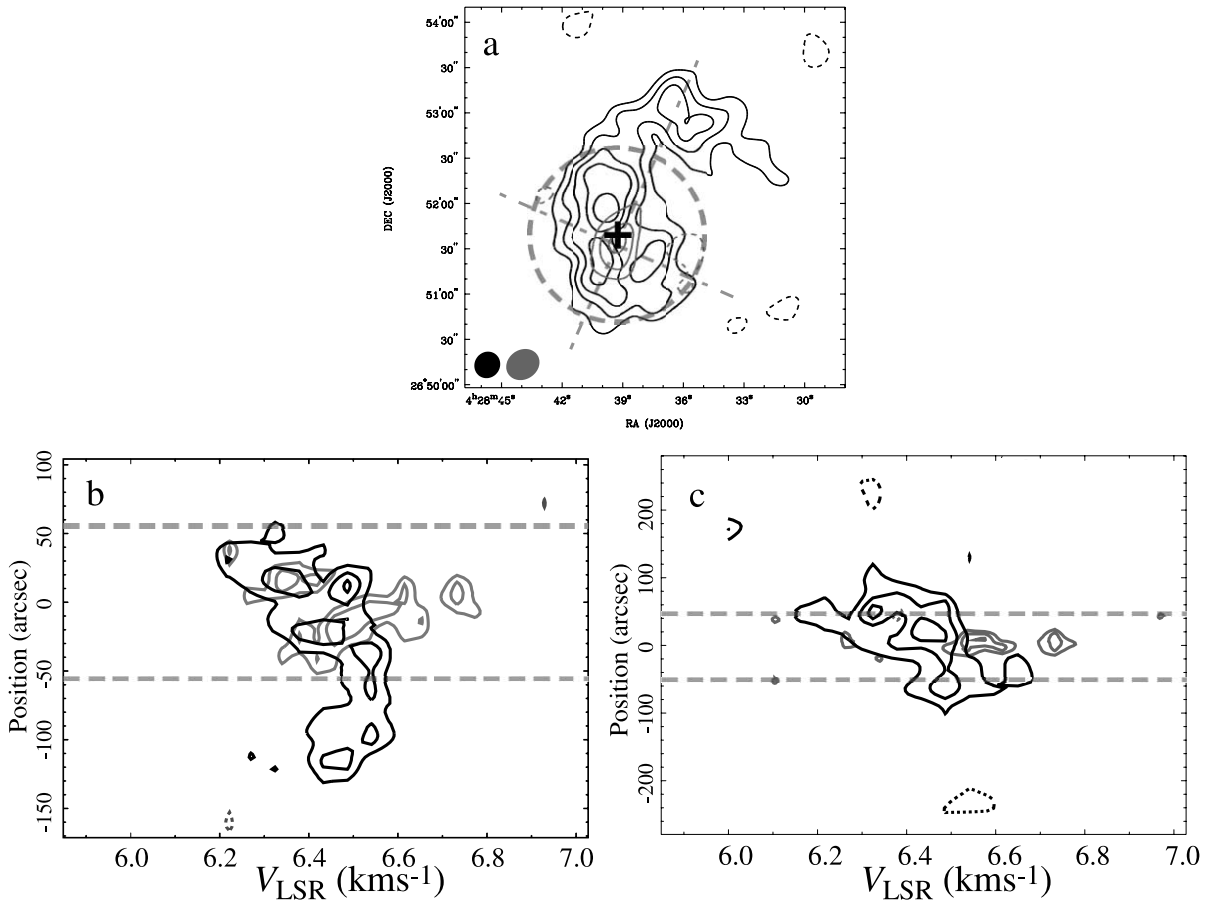


FIG. 11.—(a) Same as Fig. 2, overlaid with the major and minor axes of the fitted elliptical Gaussian to the N_2H^+ component, shown with the gray dash-dotted lines. Position-velocity diagrams of the CCS (black contour) and N_2H^+ (gray contour) components along (b) the major axis and (c) the minor axis are shown. In the diagrams (b) and (c), positions are measured from the core center traced by the N_2H^+ line. Positive in position corresponds to the east direction. The black and gray contours represent the CCS and the N_2H^+ components, respectively. The contour spacing in (b) and (c) is $\pm 1 \sigma$, starting at $\pm 2 \sigma$. Negative contours are drawn by dashed lines for each molecular component with the same colors. The dashed gray lines on the diagrams in (a), (b), and (c) represent the edge of the primary-beam half-power points of N_2H^+ imaging.

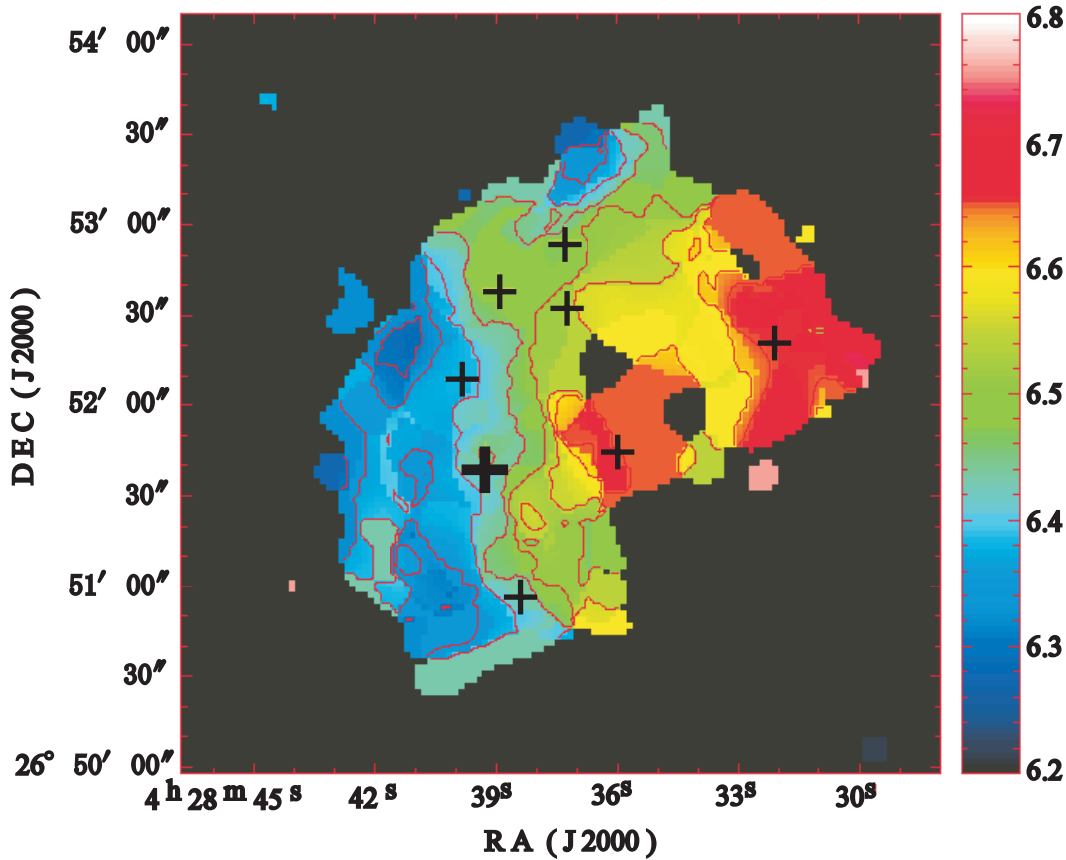


FIG. 12.—Velocity map of the CCS core brighter than 2σ in brightness. The colors indicate the velocities of the component. The global velocity gradient is observed from east to west. The big and thick cross indicates the field center. Small crosses indicate the positions of the CCS clumps.

equation (14) would be equal to $\frac{3}{5}$. However, this is much larger than the value derived from our work, and even higher than the original Kolmogorov's case. There are several possibilities that could cause this difference. For example, (1) the energy input for the turbulence may not be supplied at the largest scale, (2) the energy dissipation may not be isotropic at each scale, and furthermore, (3) the effect of the magnetic field could not be neglected, and so forth. In order to investigate more precisely, detailed observational studies are needed, including magnetic field observations of clumps and cores at different scales.

4.2. Velocity Gradient of the Core Center and the Envelope

Velocity gradients \mathcal{G} in the L1521F core are estimated and compared to the results of other cores. The velocity gradient of a clump at a distance of d is written as

$$\mathcal{G} = |\nabla v_{\text{LSR}}| = \frac{\sqrt{a^2 + b^2}}{d}, \quad (17)$$

where

$$v_{\text{LSR}} = v_0 + a\Delta\alpha + b\Delta\delta, \quad (18)$$

v_0 is the center LSR velocity of the system, and a and b are projections of the gradient per radian on the α and δ axes. As seen in § 3.2, the observational results indicate that the

rotation of the outer envelope (size ~ 0.08 pc) and that of the central compact region (size ~ 0.03 pc) are dynamically independent and that the CCS northern component would have a different dynamical center from that of the CCS southern component. Also, since the CCS northern component is dynamically independent from the CCS southern component, as shown in § 3.2, one can consider that there are three independent components that have clear velocity gradients here, i.e., the CCS southern and northern components and the major N_2H^+ component detected toward the core center. For the CCS southern component, \mathcal{G} is $7.2 \pm 1.0 \text{ km s}^{-1} \text{ pc}^{-1}$, and \mathcal{G} of the CCS northern component is $9.2 \pm 1.0 \text{ km s}^{-1} \text{ pc}^{-1}$, which is larger than that of the southern component. These are found in 0.05 and 0.04 pc scales, respectively. For the N_2H^+ component, the velocity gradient around the center is even higher than the northern CCS component, $15 \pm 2 \text{ km s}^{-1} \text{ pc}^{-1}$, found in the 0.01 pc (~ 2000 AU) scale. To compare these gradients with the other cores reported by Goodman et al. (1993), the correlation diagram between velocity gradient \mathcal{G} and R is shown in Figure 15. The top plot of Figure 15 shows the correlation between velocity gradient and size of the cores and clumps. The data are fitted by the equation $\mathcal{G} \propto R^{(1.4 \pm 0.1)}$, which is much steeper than the slope when only the other larger scale cores are considered ($\mathcal{G} \propto R^{(0.4 \pm 0.2)}$; reported by Goodman et al. 1993).

If the velocity gradient comes from the rotation of the clumps and cores, the rotational kinetic energy can be estimated and compared with the gravitational energy. The parameter β , defined as the ratio of the rotational kinetic

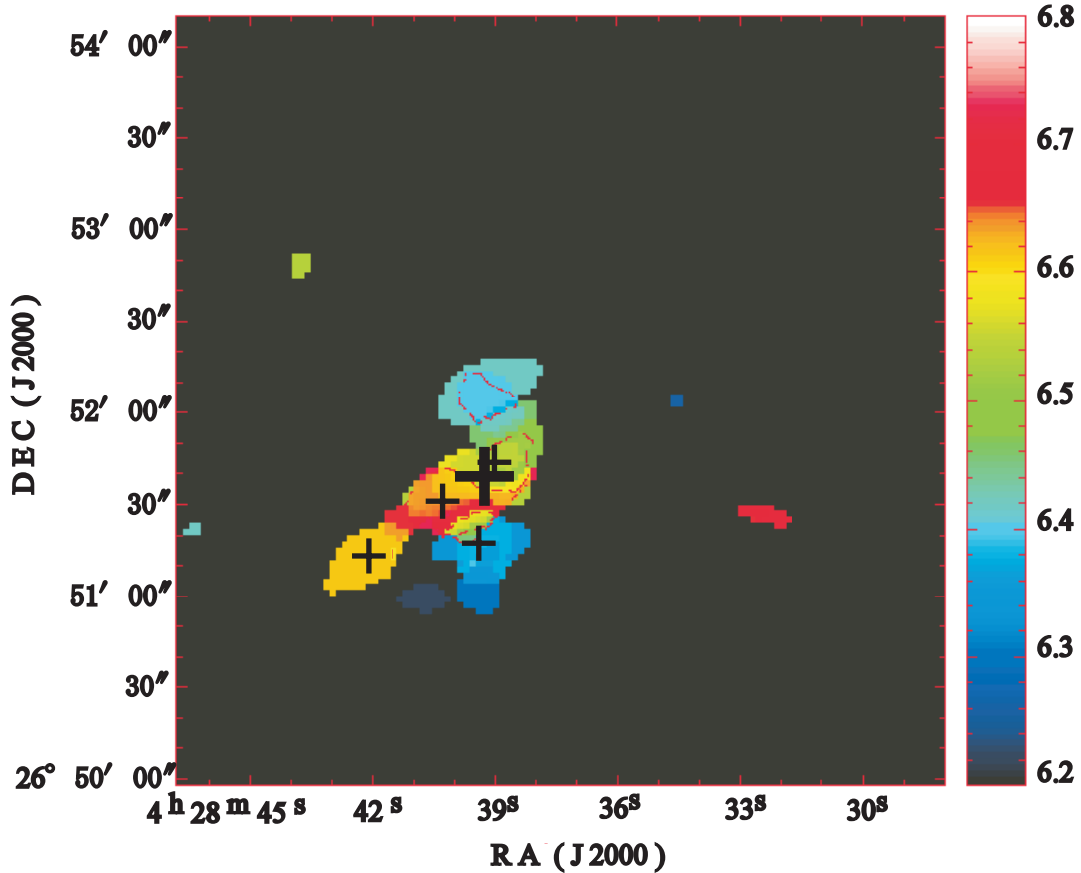


FIG. 13.—Velocity map of N_2H^+ , brighter than 2σ in brightness. The colors indicate the velocity of the component. The big and thick cross indicates the position of the field center. Around the center of the map, a velocity gradient is observed from west to east, which is in the opposite sense to the CCS global velocity gradient. The systematic velocity gradient is observed within the clump N2. Small crosses stand for the positions of the N_2H^+ clumps.

energy to gravitational energy, can be derived to infer the dynamical status in cores and clumps and can be written as

$$\beta = \frac{3}{(5-e)\gamma} \frac{\Delta v_{\text{LSR}}^2 / \sin^2 \theta}{\Delta \phi} = \frac{3}{(5-e)\gamma} \frac{(\mathcal{G} / \sin \theta)^2}{4\pi G \rho_{\text{avr}}}, \quad (19)$$

where γ is $\frac{3}{2}$ for constant density distribution, 1 for $e=1$, and 3 for $e=2$; ϕ is the gravitational potential, ρ_{avr} is average density of the core, and θ is the inclination angle to the line-of-sight direction (e has the definition described in § 3.1.3). $\sin \theta$ is assumed to be 1. The middle diagram of the Figure 15 shows the correlation between size (R) and β under constant density distribution of the cores. For the N_2H^+ clump, $\beta = 0.83$. For the southern and northern CCS clumps, the β -values are 0.26 and 0.29, respectively. For the different density distributions, i.e., $e=1$ and 2, the β -value is multiplied by $\frac{3}{4}$ and $\frac{1}{3}$, respectively. No strong correlation between β and size is found in the diagram. There may be a weak correlation in which β becomes higher when the size is smaller, but it is not clear from the results shown here.

The specific angular momentum, J/M , can be written

$$J/M = \frac{2}{5-e} R^2 \frac{\mathcal{G}}{\sin \theta}. \quad (20)$$

As seen in the equation above, the density distribution affects only the constant factor in J/M . The bottom of Figure 15

shows the J/M -size correlation when $e=0$. $\sin \theta$ is assumed to be 1 for this diagram as well. There is a strong correlation between J/M and size scale larger than 0.03 pc. However, for scales smaller than about 0.03 pc, the correlation seems to be ended, and the value $J/M \sim 0.002$ is maintained over the range. More statistics are needed to assert whether or not J/M indeed remains constant on scales smaller than 0.03 pc. No inconsistency is found in the size scale, 0.03 pc, reported by Ohashi et al. (1997) toward IRAS 04169+2702 and IRAS 04365+2535.

4.3. Chemical Evolution

To assess the evolutionary status of starless cores, it is important to take their chemical evolution into account. Suzuki et al. (1976) first established a simulation to investigate the formation of molecules in a contracting molecular cloud over a wide range of densities (from 10 to 10^7 cm^{-3}). Their results clearly showed that abundances of molecules are not in a steady state in the optically thick stages because their reaction timescales are very long ($10^{12.5}$ – $10^{13.5}$ s) compared with the contraction timescales. Following this study, many simulation studies have been done. In order to explain differences in various molecular distributions in L1544, several authors (Aikawa et al. 2001; Caselli et al. 2002; Li et al. 2002) investigated theoretically the evolution and distribution of molecules in collapsing starless cores. They found that their models could explain the observations of the L1544 core quite well. These simulations of chemical evolution models show

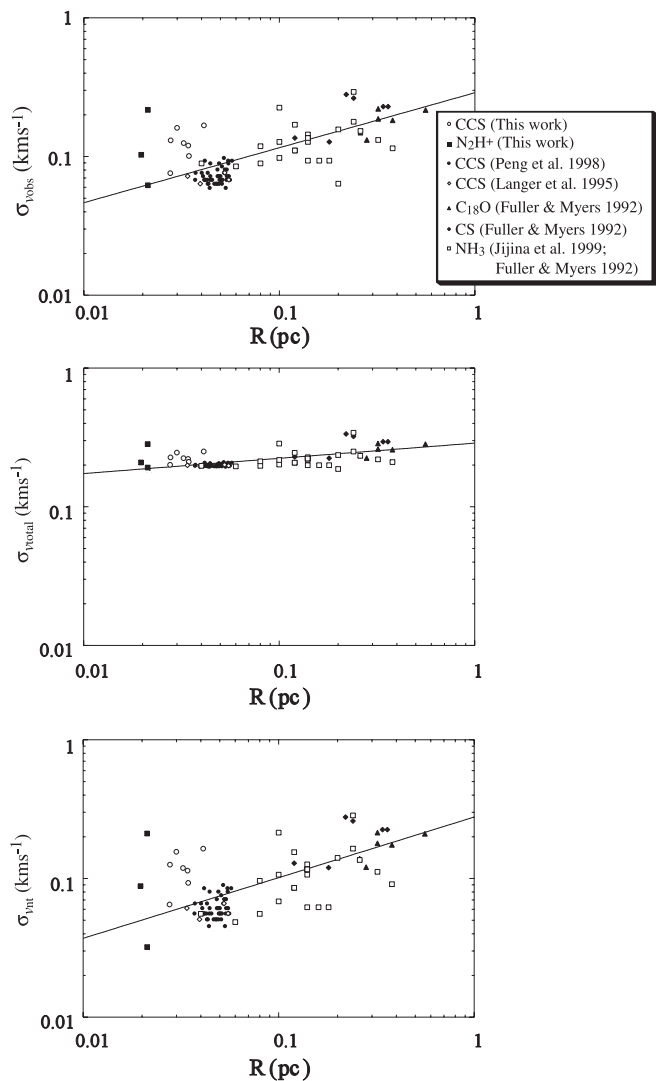


FIG. 14.—Line width—size relations toward dense cloud cores. In these diagrams, the clumps that are found in this study are compared with other dense cores and clumps reported previously by several authors (Peng et al. 1998; Langer et al. 1995; Fuller & Myers 1992; Jijina et al. 1999).

the possibility of estimating the evolutionary stages of cores by observing key molecules.

Figure 3 is the distribution of CCS and N_2H^+ from the core center, as explained in § 3.1.1. The CCS dip (hole) at the dust center may be explained by the decrease of CCS abundance because of depletion and chemical reactions. Assuming that these are the cause of the dip, one can estimate the age of the core based on chemical models. The averaged CCS density of the molecules toward the core center is estimated to be $\sim 3.7 \times 10^{13} \text{ cm}^{-2}$, assuming that the excitation temperature is 10 K. Compared with the CCS density of L1544 (Suzuki et al. 1992), that of L1521F is larger. Assuming that there is no effect from the inclinations of the asymmetric structures of both L1521F and L1544 cores, this would support that L1521F may be in a younger phase than L1544. From Figure 3, the size of the CCS dip is estimated to be $\sim 20''$, which is ~ 2.7 times smaller than that of L1544 (Ohashi et al. 1999), assuming no effect from the inclination of the asymmetric structures of the cores. If these CCS holes are created as a result of depletion and chemical reactions of the molecule, this would also indicate that L1544 would be more

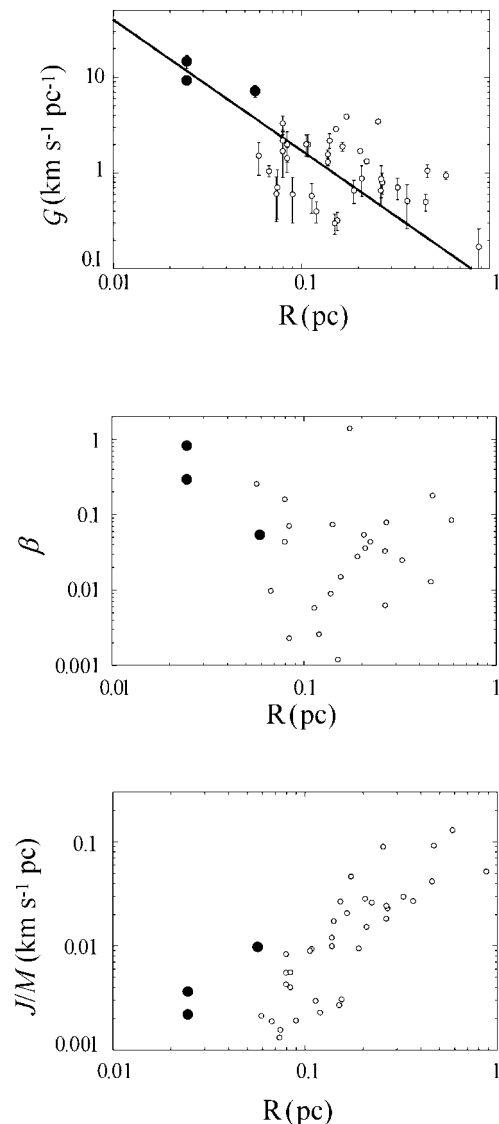


FIG. 15.—Diagrams of the correlation between size, R , and velocity gradient (*top*), β (*middle*), and specific angular momentum (*bottom*) of dense cloud cores and clumps are shown. The clumps found in this study are compared with the other cores reported by Goodman et al. (1993). The filled circles indicate the data shown in this study.

evolved than L1521F. The chemical model based on the Larson-Penston solution done by Aikawa et al. (2001) predicts that the age of L1521F is estimated to be $(1.5-1.9) \times 10^5$ yr, from the CCS density of the core center. It would be in a young phase of starless core.

Although the L1521F and L1544 starless cores look similar, there is one significant difference between them. The L1544 peak positions of the total intensity maps of the same N_2H^+ transition ($1\ 0\ 1-0\ 1\ 2$) imaging (Williams et al. 1999) and the $850\ \mu\text{m}$ dust continuum (Ward-Thompson et al. 1994; Shirley et al. 2000) have an offset ($\sim 40''$), while L1521F has the same peak for both dust and N_2H^+ . The N_2H^+ component detected in synthesis imaging is located at the position close to the northern CCS component of the imaging map (Ohashi et al. 1999). The peak position of the single-dish N_2H^+ map of the L1544 core (Tafalla et al. 1998) coincides with that of the $850\ \mu\text{m}$ continuum map ($\sim 7''$ apart), considering their pointing accuracies. The phase center of the N_2H^+ imaging of L1544 (Williams et al.

1999) is set to be at the peak position of the N_2H^+ single-dish observation of the core. If any clumpy N_2H^+ components exist at the core center, they should be detected. For L1521F, as shown in this paper, there are N_2H^+ clumps detected at the core center. The comparison between the N_2H^+ imaging result (Williams et al. 1999) and the single-dish mapping result (Tafalla et al. 1998) may indicate that the depletion of N_2H^+ has already started at the very core center of L1544 with ~ 1500 AU scale. If that is the case, this would also support that L1521F is in a younger evolutionary phase than L1544.

5. SUMMARY

High-resolution imaging observation with the CCS $J_N = 3_2-2_1$ and $\text{N}_2\text{H}^+ J = 1-0$ transitions and submillimeter dust mapping observations have been made toward a dense starless core, L1521F, in the Taurus molecular cloud. The observations show that the CCS emission well traces the envelope region of the core, $\sim 3' \times 2'$ (i.e., $0.12 \text{ pc} \times 0.08 \text{ pc}$ at 140 pc). On the other hand, the N_2H^+ components are distributed compactly ($\sim 1' \times 0.5'$, i.e., $0.04 \text{ pc} \times 0.02 \text{ pc}$), peaked at the dust continuum center. Comparing with the dust continuum, the abundances of the molecules are estimated toward the dust center and found to be similar to those previously reported toward dark cloud cores. Using the abundances, the LTE masses for each clump are estimated. The CCS molecule has a dip at the core center, which may suggest the decrease of the molecular abundance there. The channel maps of both molecular lines clearly reveal clumpy structures in the core. Furthermore, the observations reveal the multiple-kinematics structure inside the core, which has not been recognized before toward any starless dense cores. The envelope traced via CCS shows an overall velocity gradient from east to west. The

velocity gradients of the southern and northern CCS components are estimated to be 7.2 and $9.2 \text{ km s}^{-1} \text{ pc}^{-1}$ at size scales of 0.05 and 0.04 pc , respectively. On the other hand, the core center traced by N_2H^+ shows a velocity gradient from west to east, which is in the opposite sense of the global CCS velocity gradient. The N_2H^+ velocity gradient is estimated to be $15 \text{ km s}^{-1} \text{ pc}^{-1}$ at a size scale of 0.01 pc . Assuming that the velocity gradients are explained by rotation, the observational results would indicate that the rotation of the outer envelope (size $\sim 0.08 \text{ pc}$) and that of central compact region (size $\sim 0.03 \text{ pc}$) have different axes. Examining the line width–size relation of cold ($T_K \lesssim 10$) dense cores, the slope index is found to be slightly shallower than values previously reported by several authors. Assuming a spherical, uniform density sphere, the ratios of rotational to gravitational energy, β , of these cores are calculated to be ~ 0.3 for the CCS components and ~ 1.0 for the N_2H^+ core, respectively. For the specific angular momentum (J/M)–size relation, a strong correlation seen at the scales larger than $\sim 0.03 \text{ pc}$ looks terminated for the smaller scale, consistent with the results reported by Ohashi et al. (1997). On the basis of a chemical evolutionary model and assuming the depletion occurring at the core center, the age of the core is estimated to be $(1.5-1.9) \times 10^5 \text{ yr}$, which would be a young starless-core phase.

H. S. thanks Minh Choi, Ray S. Furuya, Shigehisa Takakuwa, Yancy L. Shirley, Shuro Takano, Kazushi Sakamoto, Jonathan P. Williams, Claudio Codella, Yuri Aikawa, and Masao Saito for useful discussions and/or comments and Chang-Won Lee for providing us a N_2H^+ spectra. N. O. is supported by NSC grant 92-2112-M-001-008. We thank an anonymous referee that led us to clarify many points.

REFERENCES

- Adams, F. C., Lada, C. J., & Shu, F. H. 1987, *ApJ*, 312, 788
Aikawa, Y., Ohashi, N., Inutsuka, S., Herbst, E., & Takakuwa, S. 2001, *ApJ*, 552, 639
André, P., Ward-Thompson, D., & Barsony, M. 1993, *ApJ*, 406, 122
Barranco, J. A., & Goodman, A. A. 1998, *ApJ*, 504, 207
Benson, P. J., Caselli, P., & Myers, P. C. 1998, *ApJ*, 506, 743
Carlstrom, J. E., Marshall, J., & Grego, L. 1996, *ApJ*, 456, L75
Caselli, P., van der Tak, F. F. S., Ceccarelli, C., & Bacmann, A. 2003, *A&A*, 403, L37
Caselli, P., Walmsley, C. M., Tafalla, M., Dore, L., & Myers, P. C. 1999, *ApJ*, 523, L165
Caselli, P., Walmsley, C. M., Zucconi, A., Tafalla, M., Dore, L., & Myers, P. C. 2002, *ApJ*, 565, 331
Cazzoli, G., Corbelli, G., Degli Esposti, C., & Favero, P. G. 1985, *Chem. Phys. Lett.*, 118, 164
Churchwell, E., Winnewisser, G., & Walmsley, C. M. 1978, *A&A*, 67, 139
Codella, C., Welsch, R., Henkel, C., Benson, P. J., & Myers, P. C. 1997, *A&A*, 324, 203
Crutcher, R. M., & Troland, T. H. 2000, *ApJ*, 537, L139
Dickens, J. E., Irvine, W. M., Snell, R. L., Bergin, E. A., Schloerb, F. P., Pratap, P., & Miralles, M. P. 2000, *ApJ*, 542, 870
Elias, J. H. 1978, *ApJ*, 224, 857
Fuller, G. A., & Myers, P. C. 1992, *ApJ*, 384, 523
Goodman, A. A., Barranco, J. A., Wilner, D. J., & Heyer, M. H. 1998, *ApJ*, 504, 223
Goodman, A. A., Benson, P. J., Fuller, G. A., & Myers, P. C. 1993, *ApJ*, 406, 528
Ho, P. T. P., Barrett, A. H., & Martin, R. N. 1978, *ApJ*, 221, L117
Holland, W. S., et al. 1999, *MNRAS*, 303, 659
Jenness, T., & Economou, F. 1999, in *ASP Conf. Ser. 172, Astronomical Data Analysis Software and Systems VIII*, ed. D. M. Mehringer, R. L. Plante, & D. A. Roberts (San Francisco: ASP), 171
Jenness, T., & Lightfoot, J. F. 1998, in *ASP Conf. Ser. 145, Astronomical Data Analysis Software and Systems VII*, ed. R. Albrecht, R. N. Hook, & H. A. Bushouse (San Francisco: ASP), 216
Jijina, J., Myers, P. C., & Adams, F. C. 1999, *ApJS*, 125, 161
Kolmogorov, A. N. 1941, *CR Acad. Sci. URSS*, 30, 301 (reprinted in *Turbulence: Classic Papers on Statistical Theory*, ed. S. K. Friedlander, & L. Topper, 1961; New York: Interscience)
Lada, C. J. 1987, in *IAU Symp. 115, Star Formation Regions*, ed. M. Peimbert & J. Jugaku (Dordrecht: Reidel), 1
Langer, W. D., Velusamy, T., Kuiper, T. B. H., Levin, S., & Olsen, E. 1995, *ApJ*, 453, 293
Larson, R. B. 1969, *MNRAS*, 145, 271
———. 1981, *MNRAS*, 194, 809
Lee, C. W., Myers, P. C., & Tafalla, M. 1999, *ApJ*, 526, 788
Lee, J.-E., Evans, N. J., II, Shirley, Y. C., & Tatematsu, K. 2003, *ApJ*, 583, 789
Li, Z.-Y., Shematovich, V. I., Wiebe, D. S., & Shustov, B. M. 2002, *ApJ*, 569, 792
McLaughlin, D. E., & Pudritz, R. E. 1997, *ApJ*, 476, 750
Mizuno, A., Onishi, T., Hayashi, M., Ohashi, N., Sunada, K., Hasegawa, T., & Fukui, Y. 1994, *Nature*, 368, 719
Murakami, A. 1990, *ApJ*, 357, 288
Myers, P. C., Ho, P. T. P., & Benson, P. J. 1979, *ApJ*, 233, L141
Ohashi, N., Hayashi, M., Ho, P. T. P., Momose, M., Tamura, M., Hirano, N., & Sargent, A. I. 1997, *ApJ*, 488, 317
Ohashi, N., Lee, S.-W., Wilner, D. J., & Hayashi, M. 1999, *ApJ*, 518, L41
Onishi, T., Mizuno, A., & Fukui, Y. 1999, *PASJ*, 51, 257
Onishi, T., Mizuno, A., Kawamura, A., Ogawa, H., & Fukui, Y. 1996, *ApJ*, 465, 815
Ossenkopf, V., & Henning, Th. 1994, *A&A*, 291, 943
Peng, R., Langer, W. D., Velusamy, T. B., Kuiper, T. B. H., & Levin, S. 1998, *ApJ*, 497, 842

- Penston, M. V. 1969, MNRAS, 144, 425
- Shirley, Y. L., Evans, N. J., II, Rawlings, J. M. C., & Gregersen, E. M. 2000, ApJS, 131, 249
- Shu, F. H. 1977, ApJ, 214, 488
- Snell, R. L. 1981, ApJS, 45, 121
- Suzuki, H., Miki, S., Sato, K., Kiguchi, M., & Yoshitsugu, N. 1976, Prog. Theor. Phys., 56, 1111
- Suzuki, H., Yamamoto, S., Ohishi, M., Kaifu, N., Ishikawa, S., Hirahara, Y., & Takano, S. 1992, ApJ, 392, 551
- Tafalla, M., Mardones, D., Myers, P. C., Caselli, P., Bachiller, R., & Benson, P. J. 1998, ApJ, 504, 900
- Tafalla, M., Myers, P. C., Caselli, P., Walmsley, C. M., & Comito, C. 2002, ApJ, 569, 815
- Ungerechts, H., Walmsley, C. M., & Winnewisser, G. 1980, A&A, 88, 259
- Ward-Thompson, D., Kirk, J. M., Crutcher, R. M., Greaves, J. S., Holland, W. S., & André, P. 2000, ApJ, 537, L135
- Ward-Thompson, D., Scott, P. F., Hills, R. E., & André, P. 1994, MNRAS, 268, 276
- Williams, J. P., de Geus, E. J., & Blitz, L. 1994, ApJ, 428, 693
- Williams, J. P., Myers, P. C., Wilner, D. J., & Di Francesco, J. 1999, ApJ, 513, L61
- Williams, J. P., & Teuben, P. 1997, BIMA Memo 56
- Yamamoto, S., Saito, S., Kawaguchi, K., Chikada, Y., Suzuki, H., Kaifu, N., Ishikawa, S., & Ohishi, M. 1990, ApJ, 361, 318